OPTICALLY SENSORIZED TENDONS FOR ARTICULATE ROBOTIC NEEDLES

A Thesis

by

ROHITH KARTHIKEYAN

Submitted to the Office of Graduate and Professional Studies of
Texas A&M University
in partial fulfillment of the requirements for the degree of

MASTER OF SCIENCE

Chair of Committee,	Seok Chang Ryu
Committee Members,	Won-Jong Kim
	Michael Moreno
Head of Department,	Andreas A. Polycarpou

August 2017

Major Subject: Mechanical Engineering

ABSTRACT

This study proposes an optically sensorized tendon composed of a 195 μm diameter, high strength, polarization maintaining (PM) fiber Bragg gratings (FBG) optical fiber which resolves the cross-sensitivity issue of conventional FBGs. The bare fiber tendon is locally reinforced with a 250 μm diameter Kevlar bundle enhancing the level of force transmission and enabling high curvature tendon routing.

The performance of the sensorized tendons is explored in terms of strength (higher than 13N for the bare PM-FBG fiber tendon, up to 40N for the Kevlar-reinforced tendon under tensile loading), strain sensitivity (0.127 percent strain per newton for the bare PM-FBG fiber tendon, 0.04 percent strain per newton for the Kevlar-reinforced tendon), temperature stability, and friction-independent sensing behavior.

Subsequently, the tendon is instrumented within an 18 Ga articulate NiTi cannula and evaluated under static and dynamic loading conditions, and within phantoms of varying stiffness for tissue-stiffness estimation. The results from this series of experiments serve to validate the effectiveness of the proposed tendon as a bi-modal sensing and actuation component for robot-assisted minimally invasive surgical instruments.

DEDICATION

To my parents,

Nithya Kalyani and Karthikeyan

ACKNOWLEDGMENTS

I would like to extend my heartfelt gratitude to my adviser, Dr. Seok Chang Ryu for his counsel, guidance, and insight through this endeavour. I also thank Dr. Nadhir Kosa, Dr. Bram Van Hoe, and Dr. Jan Van Roosbroeck of FBGS Technology GmbH, Jena, Germany for their technical support with the fiber-optics involved.

I thank Dr. Selwan Ibrahim and team at FAZ Technology, Dublin, Ireland for technical assistance with the interrogation unit. In addition, I express my gratitude to Alex Betamen, Eddie McCoy, and Richard Swindell at Precision Automated Laser Systems Inc., San Clemente, CA for their support with fabrication and troubleshooting of in-house equipment.

Lastly, my friends and fellow Aggies, Ameya R. Paranjpe, Manasa V. Hegde, and Pranjal M. Dixit for being my family away from home.

CONTRIBUTORS AND FUNDING SOURCES

Contributors

This work was supported by a thesis committee consisting of Dr. Seok Chang Ryu [advisor], Dr. Won-Jong Kim, and Dr. Michael Moreno from the Department of Mechanical Engineering at Texas A&M University.

The data analyzed for Section 5.1 was experimentally compiled by Kelly Sigmund, Undergraduate Collaborator, Department of Mechanical Engineering, Class of 2017, Texas A&M University. All other work conducted for the thesis was completed by the student independently.

Funding Sources

This research study was partially supported by Intuitive Surgical's Technology Research Grant for the year 2017.

TABLE OF CONTENTS

Page

LIST OF FIGURES

FIGURE Page

LIST OF TABLES

TABLE Page

1. INTRODUCTION

It has been two decades since the now ubiquitous surgical robot, *da Vinci* (Intuitive Surgical Inc., Sunnyvale, CA) was brought to the medical device market. Due to its clinical and commercial success, surgical robots have been considered to revolutionize clinical practice [1]. The next stage along this development path demands a push for robot-assisted minimally invasive surgery (MIS) across therapeutic modalities [2]. The challenge, therefore, necessitates functionally augmented surgical instruments and miniaturized robotic platforms that are smaller and more sophisticated than those currently available [3].

Although robot-assisted procedures using thin, long, and articulate instruments including the *da Vinci* system have profoundly influenced modern surgery, techniques using the slender tools inserted through small incisions deprive surgeons of cutaneous and kinesthetic feedback, a perception of depth, and dexterity – attributes which contribute to the ease of traditional open surgery [4]. Besides, studies suggest that when accurate instrument positioning is required and (or) when the associated structures are fragile such that trauma may have severe implications, the interaction between the tool and surrounding tissue may provide for useful sensory primitives to the operator [5] [6]. This necessity has motivated several academic circles to commit to intensive research on force-feedback within instruments for robotic surgery.

Literature classifies these studies primarily on the basis of sensor position - proximal (tool-base), distal (near tip/ joint) and at the end-effector (gripper) [7]. Notably, strain gauges and push-rod driven load-cells have been extensively investigated and constitute instruments with sensors nearer to the proximal end (tool-base) of the instrument [8] [9] [10]. Optical force sensors using fiber-bragg gratings (FBGs), capacitive wrist force sensors and mutli-axis force and torque-sensing strain gauges facilitate examples of distal

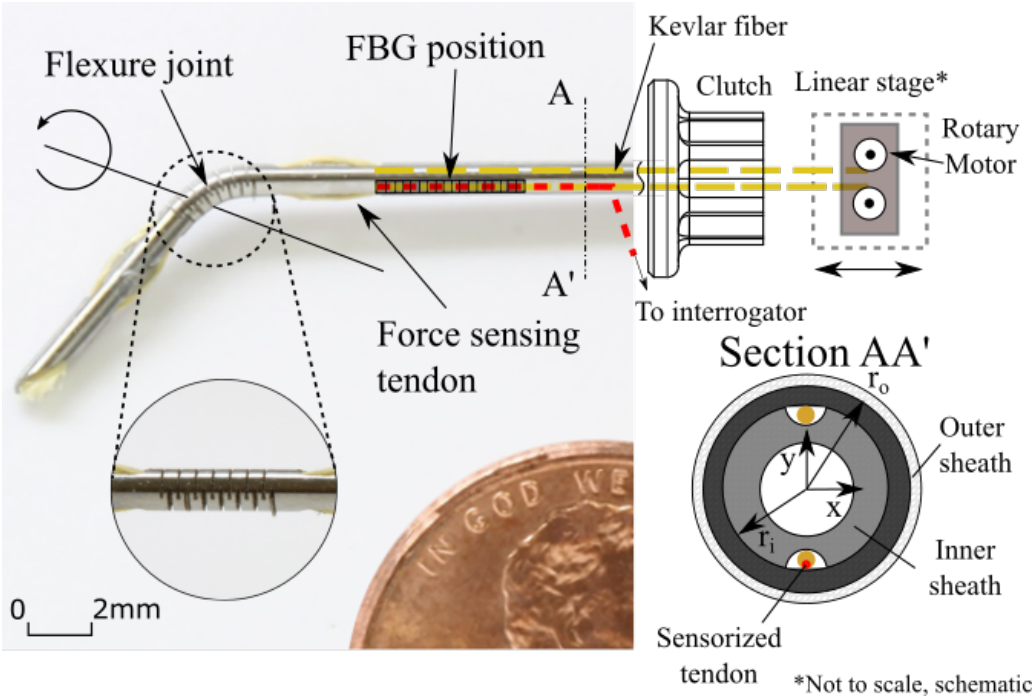

Figure 1.1: Example of the use of sensorized tendons, a force sensing steerable needle prototype with circumferential slits that enable bi-directional planar bending. The 18 Ga needle is made of a 120 mm long, 1.27 mm (0.05") diameter NiTi tube. The net range of flexion is approximately $\pm$ 29°. Section AA' depicts a cross-section with the proposed inner and outer sheaths

force-sensing methods [11] [12] [13]. Force-sensing grippers and forceps remain a common theme, including, capacitive and piezo-resistive sensors. Where, the sensors are instrumented within the end-effector [14] [15].

However, many of these alternatives are hindered by several practical limitations. Distal end sensors such as load cells are affected by mechanical hysteresis, backlash, friction and disturbance from the driving mechanism. Traditional FBGs are susceptible to temperature variations, while capacitive and piezoresistive sensors raise questions about their safety and compatibility with some imaging modalities. Grippers and the other similar end-effectors are limited by size, manufacturability and tool dexterity [16]. Hence, it is commonly acknowledged that introducing reliable sensing and actuation modalities within

such devices remains a complicated proposition, despite the fact that the desire to include such features have been expressed by an increasing number of surgeons [17].

A viable solution to these challenges would be to integrate multiple robotic functions such as actuation, sensing and joint motion within a single fundamental element. Based on this paradigm shift in robot design, we propose a unique, bi-modal approach to implementing actuation and sensing in micro-surgical procedures - *Sensorized* tendons.

In robot-assisted surgery, with end-effectors working within deep seated tissue structures and limiting workspace constraints, it is often difficult or impossible to have the actuators within the patient's body. Research on developing flexible transmission media has enabled the possibility of placing joints and actuating elements further apart [18], therefore, providing a significant advantage to the development of patient-friendly instruments for MIS using bio-compatible, safe and minimalist alternatives. Tendons as transmission elements afford the possibility of optimizing actuator position, weight, and reliability while retaining the simplicity of mechanical design and kinematics. Experiments have proven their efficiency, with tendons finding favor among robotic hands and parallel robots across research circles [19] [20] [21]. Typically, these tendons are made from stainless steel [22], polyethylene [23], and NiTi [24] cables. However, there remain a few underlying drawbacks, including – the non-negligible elasticity of the material, constraints in routing, friction from channel interaction, need for correct pre-tensioning, mechanical hysteresis and difficulties in force characterization among a few others. It is our belief that the proposed *Sensorized* tendons may offset some of these issues in practice.

A potential problem of the proposed fiber-optic tendon, however, is that the Bragg gratings are sensitive to both mechanical strain and temperature fluctuations. In the past, to negate such undesired thermal effects, additional fibers have been arranged to enable temperature compensation [25]. However, this increases tool dimensions while design choices are limited due to assumptions in support of temperature uniformity. Thus, the desired ap-

proach is to employ a particular class of fibers which allow for decoupled temperature and strain measurement from a single FBG sensor.

This thesis proposes a sensing and transmission alternative using polarization maintaining (PM) optical fibers and Bragg gratings manufactured using the Draw Tower Grating (DTG) technology. PM fibers facilitate the decoupled measurement of temperature and strain as recorded by Bragg grating sensors [26]. Therefore, real-time, localized strain and force measurements near the joint mechanism are possible without the need for temperature compensation. With the absence of reliable feedback mechanisms in robot-assisted surgery, the surgeon is compelled to rely on visual cues to guide complex procedures. Although visual-aids permit most surgical procedures at this time, the learning curve associated with robot-assisted surgery, and its subsequent expansion across therapeutic modalities demands a breakthrough [10]. To address this void, the sensorized tendon is tested within an 18 Ga x 120 mm steerable NiTi cannula with an embedded flexural joint as shown in Fig. 1.1. This aids in its performance evaluation within the context of stiffness estimation and force-sensing in robotic catheters.

The proposed thesis document will be organized as described, *Section II* highlights the background relevant to the proposed concepts along with a review of pertinent literature. *Section III*, describes the research objectives, and scope of this project, followed by *Section IV*, where, an evaluation of the performance capabilities of optical fibers as transmission elements in robot-assisted MIS is detailed. *Section V* will describe the mechanics and kinematics of the needle prototype as one of the target applications. In *Section VI*, the performance of the instrumented prototype will be evaluated, with relevant discussions. And lastly, a summary of key results, closing statements, and conclusions in *Section VII*.

2.1 Review of Optical Elements

2.1.1 Strength of Fiber Bragg Grating Sensors

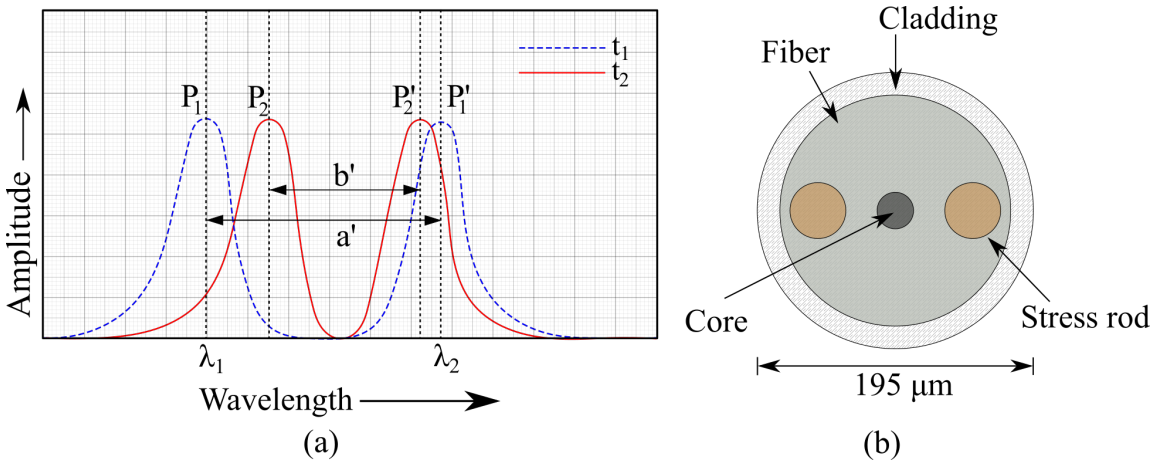

Figure 2.1: (a) Typical spectral response of a single PM-FBG fiber. a' is the peak separation at time t_1 and b' at time t_2. The relative peak shifts are shown for both $P1$ and $P2$. The instantaneous peak separation relates to temperature, while their temporal difference is proportional to fiber strain. (b) Cross-section of the PM-FBG fiber (panda-section).

In tendon driven robots, force or torque limitations are a concern owing to the properties of the material involved. The rudiments of traditional surgery may be classified as grasping, spreading, sweeping, pushing, and lateral retraction with studies estimating the required force magnitude at 1.32 N (Gall Bladder) to 3.47 N (Liver) for probing, between 1.49 N (Gall Bladder) to 3.26 N (Liver) for punctures, and up to 7.19 N for suturing (depending on the tightness of knot) [27]. Hence, the load bearing capacity of the tendons play an important role. In FBGs, strength is contingent on the technique used for fabrication [28] [29].

Traditionally, there are four steps to the FBG fabrication process: (i) removal of the fiber coating (ii) photo-sensitization (iii) exposure to UV light (irradiation of the fiber) (iv) annealing (or) re-coating. Each of these steps may progressively contribute to structural flaws on the glass surface, thereby, weakening the ultimate strength and reducing its long-term reliability [30]. Sometimes the decrease in strength could be as high as 72% , causing the fibers to break at strains lesser than 1% [31].

The advantage of an FBG sensing array is realized only if the high inherent strength and reliability of an optical fiber is not compromised during the manufacturing process [32]. In this approach the FBGs are inscribed onto the uncoated fiber during the extrusion process which offers greater fiber strain margins, and hence higher loads in tension [33].

Notably, in [33] the authors provide evidence to suggest that the strain behavior of fibers with Type-1 gratings and the Organic Modified Ceramic (OrMoCer) coating to be nearly similar to that of standard (no-grating) fibers. The estimated failure load is at $55-70$ N for gratings manufactured in this manner, and at 20 N for Type-2 gratings with a cross-section of 125 μm. The types here correspond to the ionization threshold of the glass substrate. Type-2 gratings are favored for their temperature stability.

Therefore, commercial draw tower grating PM-FBG fibers have a projected tensile load limit of 20 N, i.e. approximately one-third the permissible load on an equivalent glass fiber rod with an observed elongation grater than 3% at failure [30].

2.1.2 The Draw Tower Grating Process

As described previously, the fabrication technique determines the mechanical capabilities of the optical fiber bragg grating sensors. Research shows that the simultaneous inscription of the Bragg gratings during the extrusion process preserves the mechanical strength and enables the manufacture of Type - II gratings with the desired temperature stability. This is a consequence of the fact that grating inscription is during the window

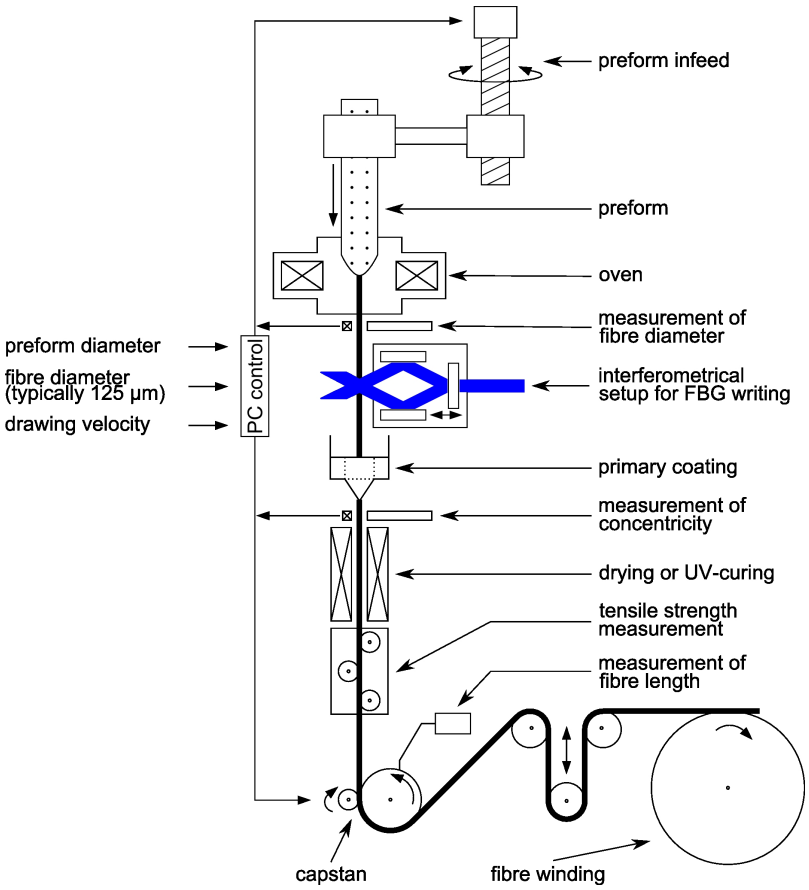

Figure 2.2: Draw tower gratings: The manufacture of Bragg grating sensors during the extrusion process. *Courtesy of FBGS Technologies GmbH, Jena, Germany*.

of time between preform melting and fiber coating. In doing so, the need for fiber removal is avoided, therefore, increasing it's performance. Empirical studies indicate that the achieved mechanical stability of draw tower gratings (DTGs) is similar to fibers without gratings.

Fig. 2.2 describes the fabrication method. The input here is a glass preform.The heated preform is drawn through molds as shown. Subsequently, the fiber meets the optical axis of the laser source and interferometer used to create a UV-light based interference pattern on the glass substrate. A pulse selector takes into account drawing speed and accurately

positions the FBGs. Following this step a coating reservoir coats the fiber, this retains the pristine fiber strength of the optical fiber.

2.1.3 Principle of Polarization Maintaining FBG Fibers

The ability to decouple strain from temperature has been explored using Bragg gratings written on highly-birefringent fiber in conjunction with accurate interrogation techniques [26]. The PM-FBGs have double Bragg reflection peaks (Fig. 2.1 (a)), which enable the decoupled measurement of strain and temperature. They are unique in their ability to decouple strain data from temperature effects. This combines the sensing attributes of traditional FBGs with the temperature independence of the PM fibers.

The PM fibers are fabricated by introducing linear birefringence into the glass substrate. The birefringence is stress-induced using stress rods along the cross-section of the extruded fiber. This preserves the polarization state of the transmitted wavelength provided the light beam is aligned with either axis of birefringence. In general, a tunable LASER interrogator platform transmits polarized wavelengths and the reflected spectrum consists of two peaks, alternatively sampled by the optical interrogator at an optimum frequency, for loss-less data acquisition.

Interestingly, the response of the dual wavelength spectrums to temperature and strain is similar to that of the FBGs. However, the sensitivities of individual peaks differ [34]. In Fig. 2.1, the reflection magnitude and corresponding spectral wavelengths are illustrated and the two reflected wavelength amplitude peaks are evident. The plots are a result of consecutive sampling instances at time t_1 and t_2. Here, a represents peak separation at time instant t_1 while the peak separation is b at time t_2. Calibration studies indicate that the separation between peaks $P1$ and $P2$ corresponds to temperature fluctuations while strain is inferred from the relative change in peak wavelengths i.e the difference between a and b [35].

The cross-coupling between temperature and strain is resolved due to this induced stress birefringence. The response of individual wavelengths λ_1 and λ_2 to strain ϵ and temperature T is described by the equations that follow.

$$\lambda_1 - \lambda_{10} = A\Delta T + B\Delta\epsilon$$

$$\lambda_2 - \lambda_{20} = C\Delta T + D\Delta\epsilon \tag{2.1}$$

$$\Delta T = (A\Delta\lambda_1 - B\Delta\lambda_2)/k$$

$$\Delta\epsilon = (C\Delta\lambda_1 - D\Delta\lambda_2)/k \tag{2.2}$$

where $\Delta\lambda_1$ and $\Delta\lambda_2$ are the change in peak wavelengths with respect to a reference wavelength at known temperature and strain. The sensitivity parameters A, B, C, and D for ϵ and T are derived empirically , while $k = AD - BC$ [35] .

2.2 State of the Art

There are three fundamental aspects to this study - sensing, actuation, and needle tip articulation. The subsequent sections briefly outline some literature relevant to these areas.

2.2.1 Sensing in Robotic Surgery

In robotic surgery, the physicians ability to feel forces acting on the end-effector is limited during the insertion and manipulation of the instrument as it punctures/ traverses within tissue layers. Force sensing is particularly advantageous to microsurgery (scaling), suturing, palpation, and robotic force control [36] [37] [38]. In addition, haptic cues during membrane puncture, interaction with oclivities, and the presence of tissue inconsistencies are valuable primitives to the operator. Such information could effectively determine tool

path and subsequent corrective strategies necessary for the success of the intervention procedure. This has motivated research on incorporating sensing modalities within surgical tools. Several of these tools are classified on the basis of sensor position - at the end-effector/ gripper, tool shaft or distal section, proximal shaft, and near the tool base [17]. In this research, the sensorized tendons permit variation in sensor location, contingent on the objectives of a specific experiment or procedure.

2.2.2 Tendon Driven Instruments for Robotic Surgery

Research on developing flexible transmission media has enabled the possibility of placing joints and actuating elements further apart [18]. Tubes, tendon sheaths, and pulleys allow cables to transmit force and position information to remote segments of the instrument. This provides for a significant advantage in the development of patient-friendly, minimally invasive surgical instruments. Tendon based transmission systems greatly simplify the mechanical design of tools used in robotic surgery. Inspired from biology, tendons as transmission elements have been studied for the development of robotic hands [19] [21]. In robotic surgery, with end-effectors working within deep seated tissue structures and limiting workspace constraints, it is often difficult or impossible to have the actuating elements (motors) within the patient's body. Tendon driven systems permit the required diversity in tool dimensions [39] [40] and offer a workaround to allow for miniaturization, safety and flexibility within a wide range of applications - the *da Vinci* [41], endoscopes [42], slave-master systems [43], etc. Therefore, the proposed optically sensorized tendon could prove a viable extension to existing tendon-driven instruments in robotic surgery.

2.2.3 Design for Needle Articulation

Needle steering in current literature refers to the possibility of actively reconfiguring the mechanical design of the needle's structure, enabling directional steering of the instrument through layers of tissue [44]. Literature classifies these approaches primarily

as active or passive depending on the extent of control available at the operator's end. Passive steering techniques include base manipulation [45], and bevel-tip steering [46], where, the initial orientation and geometry of the needle's tip together with insertion velocity and medium stiffness determine the path taken. Active steering refers to the controllable change in the needle's path by altering the structure or manner of interaction with surrounding media. Techniques include, concentric tubes that can telescope relative each other [47], pre-curved stylets that incorporate bent structures [48], reconfigurable bevel tips that alter the needle's tip [49], and tendon driven compliant cannula among others. In this study, the steering was achieved with a needle cannula having circumferential slits near the distal section, these slits reduce the stiffness across the member while enabling planar bending.

2.3 Research Objectives

The crux of this study deals with verifying the feasibility of high strength PM-FBG fibers as a bimodal actuation and sensing component in robot-assisted MIS. A series of experiments were performed to first, evaluate the performance of the sensorized tendon itself followed by testing within a prototype surgical instrument (steerable cannula - bidirectional planar bending Fig. 1.1). Subsequently, we present evidence to substantiate tendon performance in terms of strength, strain independence, and friction decay along with instrument force and stiffness sensitivity. To this end, we define the following metrics to justify this proposition.

1. Performance evaluation of sensorized tendons

    i *Tendon strength*: define load thresholds and identify modes of failure.

    ii *Temperature-strain decomposition*: experimentally validate this independent relationship.

iii *Friction compensation*: quantify transmission decay with friction and draw parallels with existing theory.

iv *Effect of Kevlar reinforcement*: characterize the strain behavior in optical fibers reinforced with synthetic para-aramid fibers (Kevlar).

2. Experimental validation of proposed application

i *Kinematics and mechanics - system analysis*: estimate tip flexion, range of motion, workspace, and bending behavior of test prototype.

ii *Response to static loads*: calibrate for reaction force and stiffness by observing static strain behavior during flexion within homogeneous phantom tissue.

iii *Response to dynamic loads*: observe and characterize the behavior of the sensorized tendons and prototype under the influence of dynamic forces.

iv *Tissue stiffness estimation during phantom insertion*: observe and characterize strain response during insertion within multi-layered phantom tissue, and real-time tissue stiffness estimation.

Given the above premise, there are certain limitations to this study. Firstly, the lack of real-time control using fiber data limits steerability. Phantom behavior is visco-elastic and the working assumptions for stiffness estimation require further substantiation. The proposed application comprises of a single PM-FBG fiber which inhibits exact decomposition of force information and bi-directional tip control. Moreover, the design of the flexure itself is not optimized toward efficacy in stiffness estimation. Location, geometry, flexibility, and strength should be studied further for its safe use as a steerable medical device. Therefore, these aspects signal plausible future directions for the proposed concept. The experimets, results, and subsequent discussion present evidence in support of the defined objectives within the confines of the stated limitations.

3.1 Comparison Under Tensile Load

To discern the safe loading conditions for the actuating fibers (PM-FBG fibers, FBGS International, Brussels, Belgium), standard gauge optical fibers used in tele-communication (Nufern Inc, CT, USA) were subject to tensile loading. Three fibers were tested with incremental load applied over consistent time intervals and strain rates. The loads at failure were then recorded.

A bench-top tensile-testing machine (Instron 4411, Instron Corporation, United Kingdom) was used for this experiment with a maximum applied load of 11.8 N over 60 s time intervals at a strain rate of 0.1 in/min. The fibers varied in cross-section (core, cladding, and coating diameters) and coating material.

Notably, the failure loads for the Nufern 1550B-HP and MMS-S105/125-22A having similar glass layer dimensions as the PM-FBG fiber was 11.8 N and 9.81 N respectively. However, they differ in terms of coating material. Coating separation was observed as a common mode of failure. The glass core remained intact across trials, i.e. jacket strip-off was observed prior to core disjunction. In Fig. 3.1 (a), the PM-FBG fiber's response

Fiber type	**Nufern 1**	**Nufern 2**	**Nufern 3**	**DTG PM-FBG**
Coating Diameter μm	245.0$\pm$15.0	165.0$\pm$10.0	245.0$\pm$15.0	195 $\pm$15.0
Cladding Diameter μm	125$\pm$ 2.0	80$\pm$1.0	125.0$\pm$1.0	125$\pm$ 2.0
Core Diameter μm	105$\pm$3.0	6.0	9.0	6.0
Failure Load N	9.81	5.4	11.8	> 13 (3% strain)
Coating Material	Acrylate	Acrylate	Acrylate	OrMoCer

Table 3.1: Results from tensile loading experiments on standard tele-communication fibers and high strength PM-FBG fibers. Where, Nufern 1 - MM-S105/125-22A, Nufern 2 - 1310M-HP-80, and Nufern 3 - 1550B-HP.

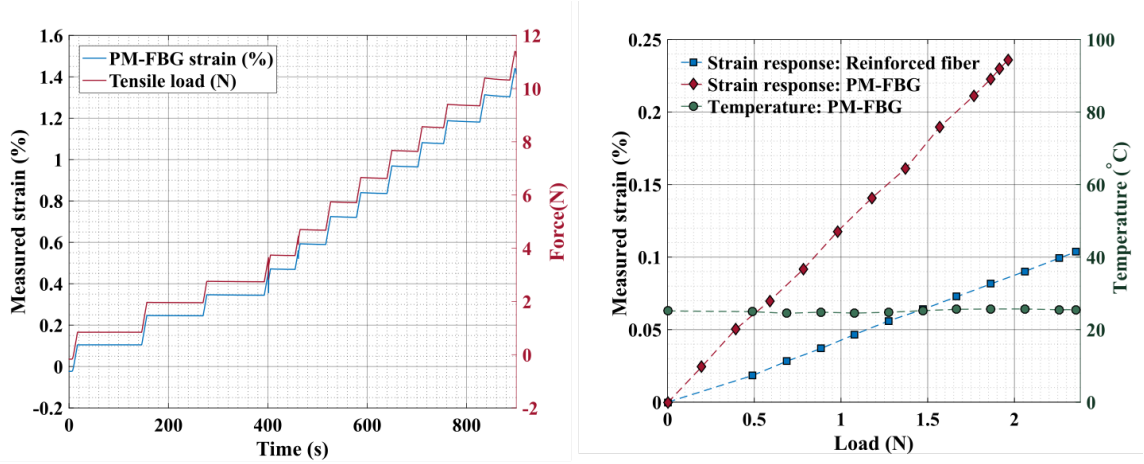

Figure 3.1: Performance evaluation of sensorized tendons (a) Tensile load limit and time-sensitivity as observed for the PM-FBG fibers. (b) Strain and temperature response of a bare PM-FBG fiber and Kevlar reinforced fiber under tensile loading.

to tensile load is documented, the load limit is constrained to approximately 12 N due to wavelength limitations of the interrogator. The fiber response remained consistent and error-free after repeated trials beyond the required duration, no fracture was observed up to this load.

Vendor documentation projects a failure load of 20 N for the PM-FBG fibers. Table 3.1 further details the results from these tests, evidently, the PM-FBG fiber is able to withstand loads greater than a standard tele-communication fiber (no FBGs) having slightly larger cross-sectional dimension, this is potentially attributed to the special coating used.

3.2 PM FBG Strain Response and Sensitivity

To calibrate the PM-FBG fibers and to test their strain sensitivity i.e. percent strain per unit load in tension (%/N), load tests were performed using standard weights and a bench-top tensile test setup. The optical fiber was connected to the interrogator (FAZ Technologies Inc., Dublin, Ireland) and the free-end bonded to a 3D printed attachment. A section of the fiber was taped onto a support structure while loads were suspended from

the free end. Considering a 20 N failure load, a factor of safety of four was adopted as the safe load limit for fibers in subsequent experiments (4.905 N for time intervals < 300 s). Two trials were performed with load increments of 20 g up to 200 g and another with load steps of 50 g up to 500 g at room temperature (27 °C). The peak wavelength shifts were recorded using the system GUI (Femto-sense, FAZ Technologies, Dublin, Ireland) and post-processed for strain and temperature information. A plot of load to strain and temperature was obtained as shown in Fig. 3.1 (b), this served as a reference source for calibration in future experiments.

The above process was repeated with Kevlar-reinforced PM-FBG fibers. The optical fiber is bonded using an instant alkoxy-ethyl adhesive (Loctite 403, Henkel Adhesives, USA) to a strand of pre-tensioned synthetic para-aramid fiber (Kevlar, DuPont, Wilmington, DE) as shown in Fig. 3.2. The bonding length was 10 mm and the cure time 24 hrs. In doing so, the bonded section can be modeled as a simple composite bar in axial tension. Here, T_{net} is the applied tension that results in an extension, δL_b across each layer such that,

$$(\delta L_b)_{Of} = (\delta L_b)_{Ad} = (\delta L_b)_{Kev} \tag{3.1}$$

$$\left(\frac{TL_b}{AE}\right)_{Of} = \left(\frac{TL_b}{AE}\right)_{Ad} = \left(\frac{TL_b}{AE}\right)_{Kev} \tag{3.2}$$

where, T corresponds to the applied load across the section, L_b - length of the bonded segment, A - the area of cross-section and E - elastic modulus of the material. Of refers to the optical fiber, Ad - adhesive and Kev - Kevlar fiber. The elastic modulus for kevlar (E_{kev}) is taken as 110 GPa, the optical fiber - E_{Of} as 16.56 GPa and the adhesive - E_{Ad} as 3.67 GPa [50] [51].

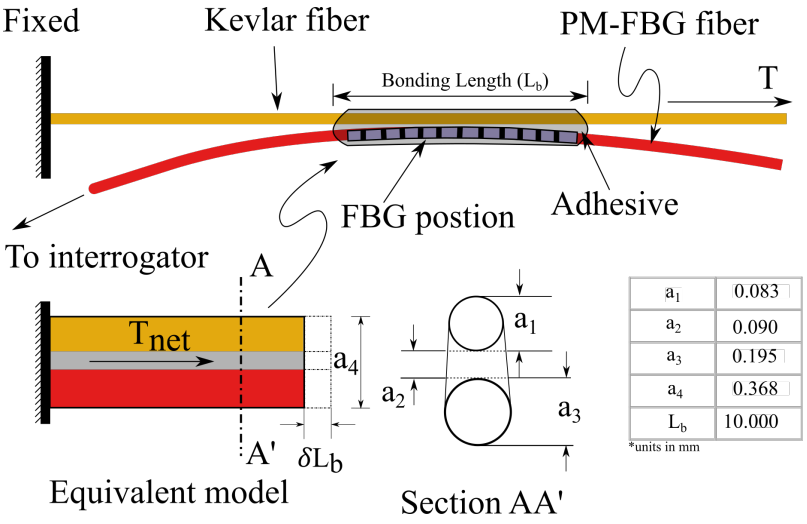

Figure 3.2: Schematic depicts the the PM-FBG fiber reinforced with pre-tensioned Kevlar fiber. Equivalently modeled as a composite bar under axial tension with Kevlar and optical fiber regions separated by an exaggerated adhesive layer.

Therefore,

$$T_{net} = 2.8123 T_{Of} \approx 3(T_{Of}) \tag{3.3}$$

This implies that the effective load experienced by the optical fiber when reinforced with Kevlar is approximately one-third the magnitude of load applied to the Kevlar fiber itself. This extends to the possibility that when reinforced, the sensorized tendons can carry up to three times the permissible load for the bare PM-FBG fiber. This claim is validated experimentally in the sections to follow.

3.2.1 Bare Fiber

The plot in Fig. 3.1 (b) represents the strain to load relationship (strain-response) for the bare PM-FBG fibers while under a tensile load. The response is seemingly linear with a sensitivity of 0.1266 %/N. The temperature stability of the fiber is apparent as evidenced

by the simultaneous temperature data plot, with room temperature at $26°$C as determined using a thermometer. This relationship was consistent over three trials. The applied load was increased to a maximum of 4.9 N under a strain rate of 0.1 in/min.

In Fig. 3.1 (a), the bare PM-FBG fiber was subject to tensile load increments of 1 N up to $\sim$ 12 N with a time interval of 60 s each. The fiber response was unaffected and remained consistent across trials. This lends support to the idea that the PM-FBG fibers could function as efficient transmission media in applications that require small loads up to a cut-off value.

3.2.2 Kevlar-reinforced Optical Fiber

The plot in Fig. 3.1 (b) also depicts the relationship between strain and applied load for the PM-FBG fibers when reinforced with Kevlar fiber having a nominal diameter of 250 μm. The reinforced fiber bundle has a load sensitivity of 0.03975 $\%$/N. The temperature stability of the fiber is evidenced by the simultaneous temperature data plot, with room temperature at $26°$C as measured using a thermometer.

Notably, the observed strain dropped by about 35% during these trials which is approximately equivalent to the expected difference (Eq. (5)). This can be attributed to the idea that the bare fiber, the adhesive and the synthetic fiber now function like a composite with a certain degree of load re-distribution as described theoretically from Fig. 3.2. This relationship was consistent over three trials. A maximum load of 11.8 N was applied at a strain rate of 0.25 in/min.

For applications involving large loads, Kevlar can be used as a force carrying tendon while the PM-FBG fiber is bonded to it. Kevlar fiber has a higher stiffness than the PM-FBG fiber and hence undergoes lesser strain for the same load, this permits up to three times the load carrying capacity of bare fiber (approx. 40 N). This tensile load capacity translates to a lateral force magnitude of approximately 5.08 N (as detailed in Section

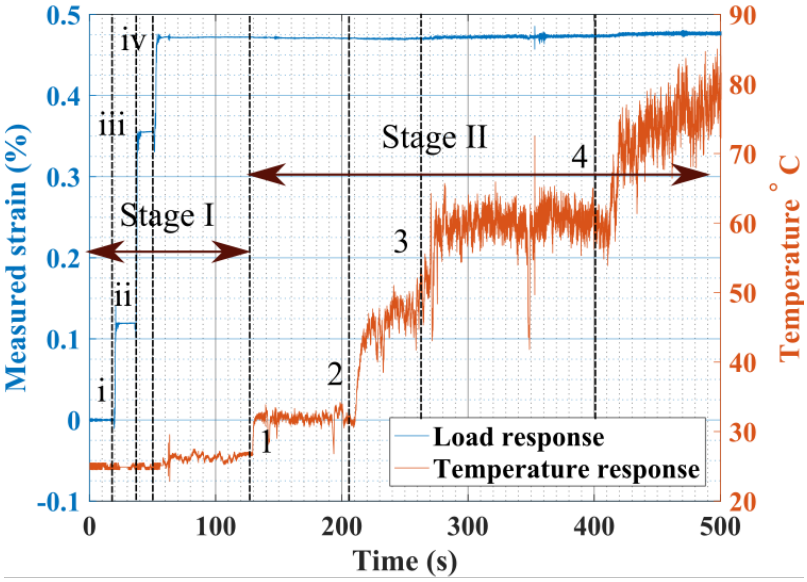

Figure 3.3: Temperature independence of the PM-FBG fiber: During Stage I - constant temperature and incremental load up to 500 g. Stage II - constant load (strain) increasing temperature from 27°C (ambient) to approx. 90°C. Note: temperature axis is to the right.

V-B) which is sufficient for most rudiments of modern surgery [27]. Equivalently, for a device such as the EndoWrist, with a cross-sectional diameter of 8 mm, and gripper length 10 mm this could be enhanced up to 31 N in terms of grasping force at the end-effector. Moreover, due to limitations in the bend radius of the glass core in an optical fiber, reinforcing elements such as Kevlar enable unique tethering configurations advantageous to the specific application.

3.3 Temperature Independence of PM-FBG Fibers

Fig. 3.3 demonstrates the temperature independence of the sensorized tendons. This experiment was performed in a controlled environment. During Stage-I, the optical fibers were placed in a stress-free state at room temperature ($26°C$). Loads were then added to the bare fiber in four steps up to 400 g i.e. steps i to iv. As evidenced by Fig. 3.3, the temperature readings remain consistent throughout this stage while, strain rises in response to increasing load.

In Stage-II, the optical fibers were under a constant tensile load ($400g$) while ambient temperature was increased in four stages using a heat gun and a thermally reflective enclosure. Temperature was gauged in tandem with wavelength using a thermometer. Step 1 corresponds to a nominal temperature of 32 °C, step 2 at 45 °C, step 3 at 60 °C and step 4 up to 80 °C (as measured). Notably, the noise in strain data beyond a certain temperature step is attributed to the draft induced by the heat gun.

This experiment clearly demonstrates the idea that the temperature response of the grating is independent of applied load. Moreover, the measured temperature was in agreement with the observed temperature as determined using an external thermometer. This validates the temperature independence of the wavelength shifts registered by the PM-FBG fiber. Therefore, undesired thermal effects would not hinder the performance capabilities of the sensorized tendons.

3.4 Friction Effects: Transmission Decay

This section details the influence of friction on tendon based force transmission and how fiber-optic sensing provides means to quantify this attribute. Under tendon actuation, an important concern is force reduction due to friction loss. Research by Palli et. al. [19] points to a theoretical model that postulates tendon decay as a factor influenced by two elements inherent to the transmission media: angle of curvature (θ) and the coefficient of friction (μ) between the contact surfaces (PM-FBG fiber Coating and the polytetrafluoroethane (PTFE) Lumen). Hence, higher the angle θ, higher the transmission decay.

Fig. 3.4, presents a schematic of an infinitesimal section of the tendon while under tension. The tendons are routed within the PTFE tube which is held in contact with the curved surface. Where, transmission decay is a consequence of the relative motion between the stationary lumen and moving optical fiber.

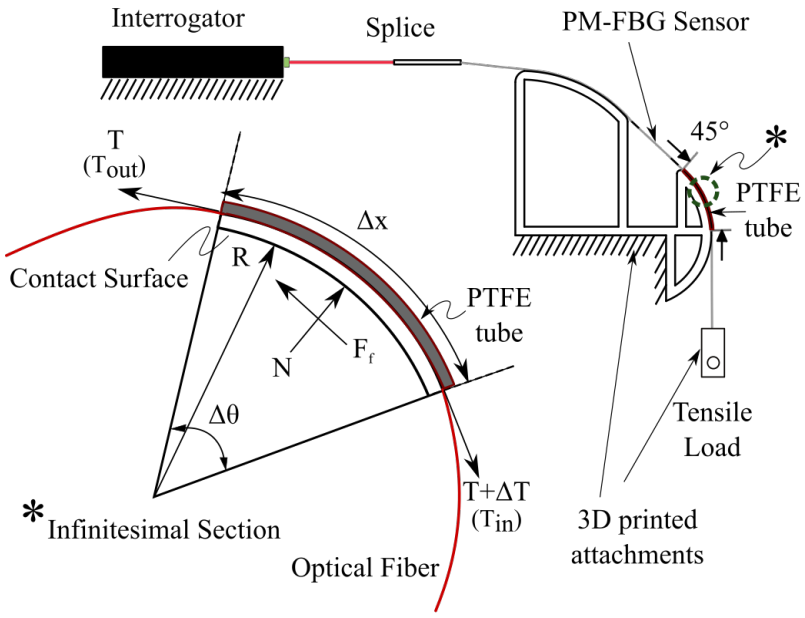

Figure 3.4: Transmission decay investigation: Force-balance on an infinitesimal tendon section in frictional contact with the PTFE lumen as observed on the experimental setup.

$$F_f = \mu N sgn(\dot{\epsilon}) \tag{3.4}$$

$$\Delta T = -F_f \tag{3.5}$$

where, F_f is the friction force, N the normal load due tendon motion and surface curvature, $\dot{\epsilon}$ the tendon deformation rate, and ΔT the loss in tension due to friction. Therefore for the infinitesimal tendon segment,

$$N = T d\theta = T\frac{dx}{R} \tag{3.6}$$

$$dT = -F_f = -\mu T\frac{dx}{R} sgn(\dot{\epsilon}) \tag{3.7}$$

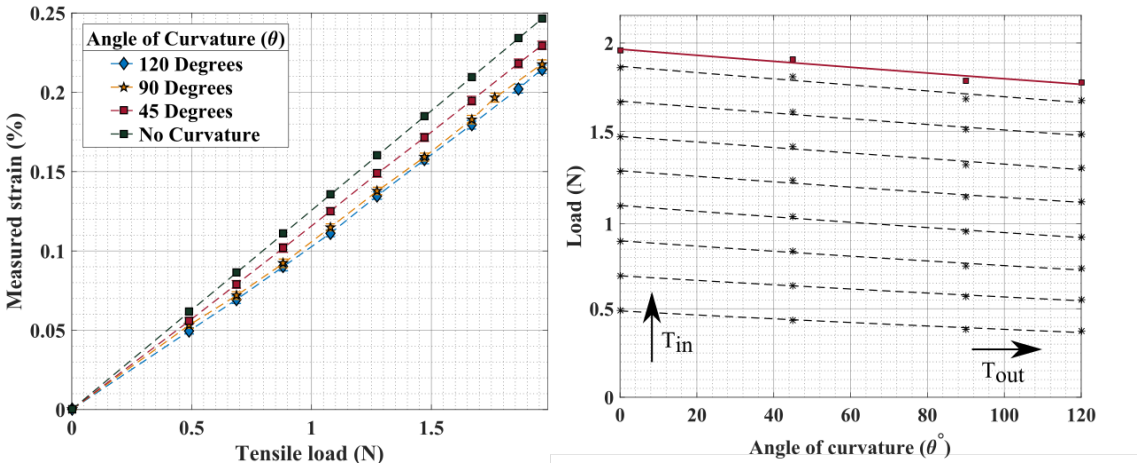

Figure 3.5: (a) Strain response with increase in applied load for different anngles of curvature. (b) Measured load magnitude against angle of curvature and applied load, T_{in} is increased and corresponding T_{out} is depicted as a function of θ.

where, $d\theta$ is the angle subtended by the arc made by the infinitesimal section (dx). dT is the corresponding decay and R the radius of curvature. Now, Eq. (9) can be integrated over the tendon length to provide for a relationship between T_{in} (input tensile load) and T_{out} (measured tensile load) as in Eq. (10) - which depends on the direction of loading.

$$\frac{dT_{out}}{dT_{in}} = \begin{cases} e^{-\nu}, & \dot{\epsilon} > 0 \\ e^{\nu}, & \dot{\epsilon} < 0. \end{cases} \tag{3.8}$$

where,

$$v = \frac{\mu}{R} L = \mu\theta \tag{3.9}$$

Based on the coulomb friction model developed by Kaneko et. al. [52], where, transmission decay is the consequence of frictional contact between the tendon and a fixed surface, a segmented exponential function provides for a quantifiable relationship between tension output and tension input across the curved section.

This is substantiated experimentally, in Fig. 3.5 (a), a schematic of the test setup used is described. This setup was used to test for change in fiber strain with varying angles of curvature. The fibers were routed through a PTFE lumen bonded to a surface having the required angle of curvature. The FBGs were positioned so as to be devoid of contact which may interfere with the tension readings. Loads were applied at fixed intervals and the corresponding fiber strain recorded. The process was repeated for three different angles of curvature. The results so compiled were compared with the load calibration data obtained in Fig. 3.1 (b).

Due to contact between the curved surface and fibers, the effective tensile load experienced by the gratings is less than the applied load - this behavior is amplified with both increase in angle of contact and (or) coefficient of friction for the material pair. Correspondingly, the output strain decreases with increasing angle of curvature. Hence, as expected, in Fig. 3.1 (b) the fiber strains show a marked decrease with increasing angle of contact.

As the tension on the input end T_{in} is increased, the corresponding output load as determined from fiber strain is shown in Fig. 3.5 (b). Here, the load at θ set to zero corresponds to the input tension (T_{in}), and subsequent data-points relate to the measured tension (T_{out}) at different angles of curvature. This trend is potentially exponential and supports the segmented exponent idea described in existing literature [19]. This underscores the possibility that, with the PM-FBG fibers as actuating elements, the control model may circumvent the need to externally account for friction based decay in tendon driven systems. Besides, the behavioral attributes of the sensorized tendon mimic that of existing tendons in literature - a model well-understood. However, in practice, interactions between the tendon and contact channel are complicated and may not subscribe to the assumptions of existing theory - hence, an inherent sensing modality would prove advantageous. Subsequent sections discuss tendon performance within the context of the proposed application.

4. TOOL DESIGN DESCRIPTION

To better comprehend the underlying kinematics and to describe the force response of the tendons, a brief discussion of tool design is presented. The sensorized tendons studied in Section IV, when instrumented within the prototype can estimate stiffness or reaction forces during tool-tissue interactions. This demands a study of the joint kinematics and deformation behavior during bending. A prototype was fabricated using NiTi tube with an outer diameter of 0.05 in and wall thickness of 0.01 in (18 Ga). A flexure joint was embedded onto the needle by laser machining circumferential slits across a small section. The pattern so machined, enabled bi-directional flexion (bending) of the needle's tip along a plane and is labeled *bi-direction flexure*.

Two stages of actuation of the prototype are shown in Fig. 4.1. The sample used for the experiment was 120 mm long. The total length of the patterned joint was 4 mm. A section of length 6 mm was left un-patterned ahead of the joint. The schematic in Fig. 4.1 also describes tendon routing. Here, the tendons are arranged in an antagonistic manner and actuated by DC motors placed near the proximal segment of the instrument.

However, the proposed prototype is limited by the fact that there is only one sensorized tendon actuating the flexure - this hinders effective force decomposition. Besides, the design of the flexure itself is largely un-optimized and remains beyond the scope of this investigation. In addition, the approach posits the use of an inner lumen to route the actuating fibers, under the absence of which the kinematic assumptions may not hold. The subsequent results examine the performance merits of the proposed sensing modality within the confines of these limitations.

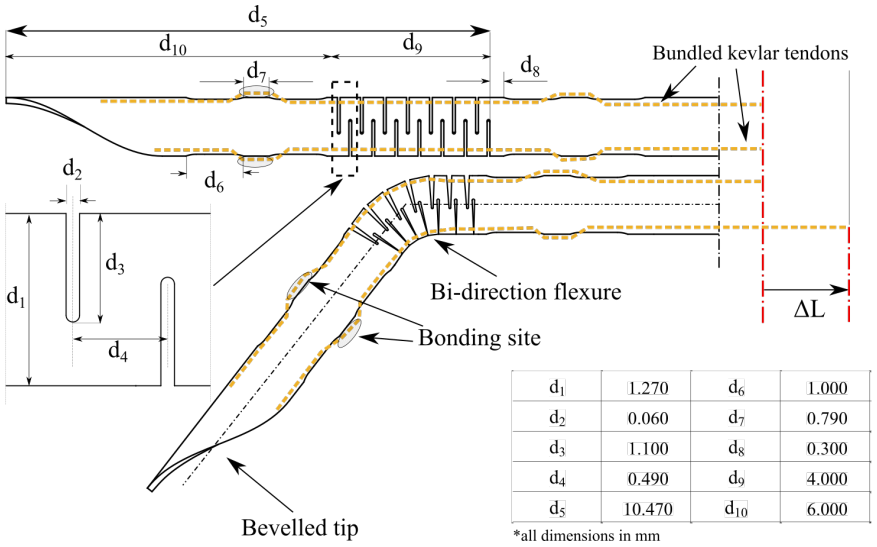

d_1	1.270	d_6	1.000
d_2	0.060	d_7	0.790
d_3	1.100	d_8	0.300
d_4	0.490	d_9	4.000
d_5	10.470	d_{10}	6.000

*all dimensions in mm

Figure 4.1: Joint kinematics for the bi-directional planar flexure: section under bending is as shown, with dimensional attributes of a single recurring section and its corresponding geometry under bending load.

4.1 Needle Kinematics

A kinematic model is described for the recurring joint segment, with frame assignments as depicted in Fig. 4.1 (a). Here, the flexure joint is assumed to undergo constant curvature bending across recurring sections of the joint. A single joint segment consists of two circumferential slits arranged opposite to one another as shown. Seven such recurring segments enable up to 29° of flexion in a given direction.

Evidence supporting this assumption has been discussed earlier in literature [53]. Further, the tendons are modeled as though they remain in contact with the walls of the cannula during the flexion process. In addition, the tendon itself is regarded as an inextensible element made of high strength Kevlar fiber [54] [55]. These assumptions remain reasonable given the material choice and design constraints.

The objective here is to map tendon extension ΔL to tip flexion θ. This requires assumptions to locate the neutral axis for the beam, as discussed previously [53]. On a

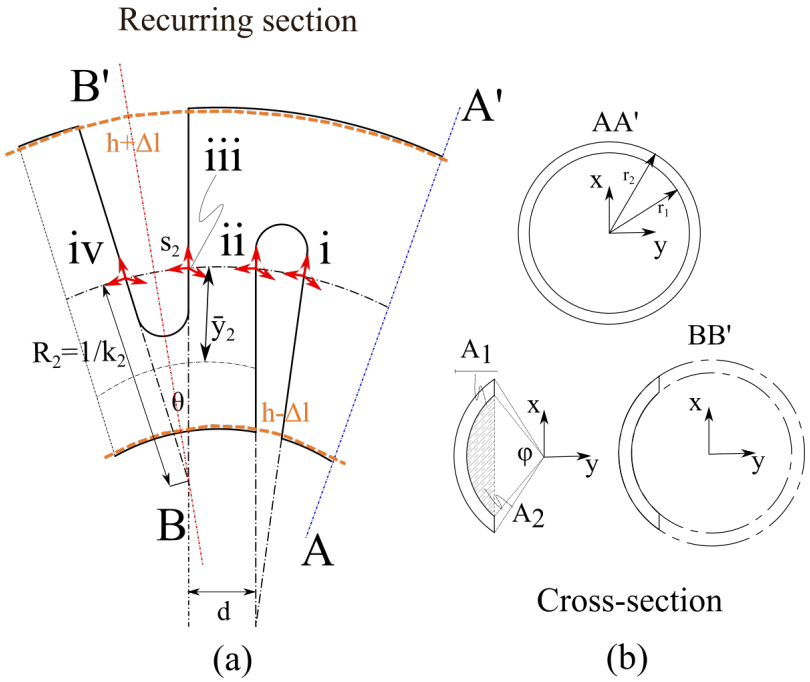

Figure 4.2: Needle kinematic description: (a) Reference frames i to iv and geometric parameters of interest for the recurring section under bending. (b) Sections AA and BB' detailed.

similar vein, we assume that the neutral axis passes through the centroid of the cross-section at each segment.

$$\overline{y} = \frac{\overline{y_1}A_1 - \overline{y_2}A_2}{A_1 - A_2} \tag{4.1}$$

Where, $\overline{y}$ is the distance of the centroid of section BB' from its center. $\overline{y_1}$ and $\overline{y_2}$ are the the centroids for sections 1 and 2 as shown in Fig. 4.2 (b), while A_1 and A_2 are their respective areas. Note, frame assignments remain consistent at each segment, therefore, depending on the orientation of the slits, the centroid position either takes a positive or a negative value.

For the joint, the cutting depth is 1.1 mm (d_3), slit separation is 0.49 mm (d_4) and a slit width of 0.06 mm (d_2). The sections BB' and AA' correspond to the slit-section and

tube cross-sections respectively. A_1 and A_2 correspond to the area of circular segments as indicated in Fig. 4.2 (b) given by Eq. (14), with corresponding centroids at $\overline{y_1}$ and $\overline{y_2}$ given by Eq. (13) [53].

$$\overline{y_n} = \frac{4r_n sin^3(1/2\phi_n)}{3(\phi_n - sin(\phi_n))} \tag{4.2}$$

$$A_n = \frac{r_n^2(\phi_n - sin(\phi_n))}{2} \tag{4.3}$$

$$\phi_n = 2cos^{-1}((g - r_n)/r_n) \tag{4.4}$$

The subscript n corresponds to section 1 and 2 for the cross-section. Based on the deformation geometry of the circumferential slits as shown in Fig. 4.2 (a), we can now map the tendon pulling length to the curvature k as described in Eq. (16) using arc equations and trigonometric identities.

$$\Delta L = h - 2(1/k - r_n)sin\left(\frac{kh}{2(1 + \overline{y}k)}\right) \tag{4.5}$$

where, h is the initial tendon length. Now, this provides equations for curvature k and arc length s i.e. the length of the actuating fiber within the deformed slit segment (Eq. (17)). From these expressions we derive a sequence of transformations from frame i to frame iv (see Fig. 4.2 (b)).

$$k_i = \frac{\Delta L}{h(r_n + \overline{y}) - \Delta L\overline{y}} \quad s_i = \frac{h}{1 + \overline{y}k_i} \tag{4.6}$$

Homogenous transformations, with angular deflection and displacement across slit 1 $(i - ii)$, followed by displacement d across the undeformed region separating the two

slits $(ii - iii)$, angular displacement and deflection across slit 2 $(iii - iv)$ and subsequent translation to the neighboring segment. These rudiments together contribute toward the net deflection of a single recurring element.

$$H_i^{iv} = \begin{bmatrix} 1 & 0 & 0 & 0 \\ 0 & cos^2(k_2 s_2) & B_{22} & B_{33} \\ 0 & -B_{22} & -sin^2(k_2 s_2) & C_{33} \\ 0 & 0 & 0 & 1 \end{bmatrix} \tag{4.7}$$

where,

$$B_{33} = \frac{-sin(k_2 s_2)(dk_1 + sin(k_2 s_2))}{k_1}$$

$$B_{22} = cos(k_2 s_2) sin(k_2 s_2)$$

$$D_{33} = \frac{cos(k_2 s_2)(dk_1 + sin(k_2 s_2))}{k_1}$$

Hence, the net transformation for a single segment is

$$H_j^{j+1} \equiv \prod_{k=i}^{iv} \{H_k^{k+1} T_z\{d\}\} \tag{4.8}$$

Therefore, for n (here, $n = 7$) such segments i.e. n: the number of segments,

$$\left\{ H_0^n \right\}_{net} = \prod_{j=1}^{n} H_j^{j+1} \tag{4.9}$$

Eq. (20) describes the kinematic model that relates tip flexion to tendon pulling length.

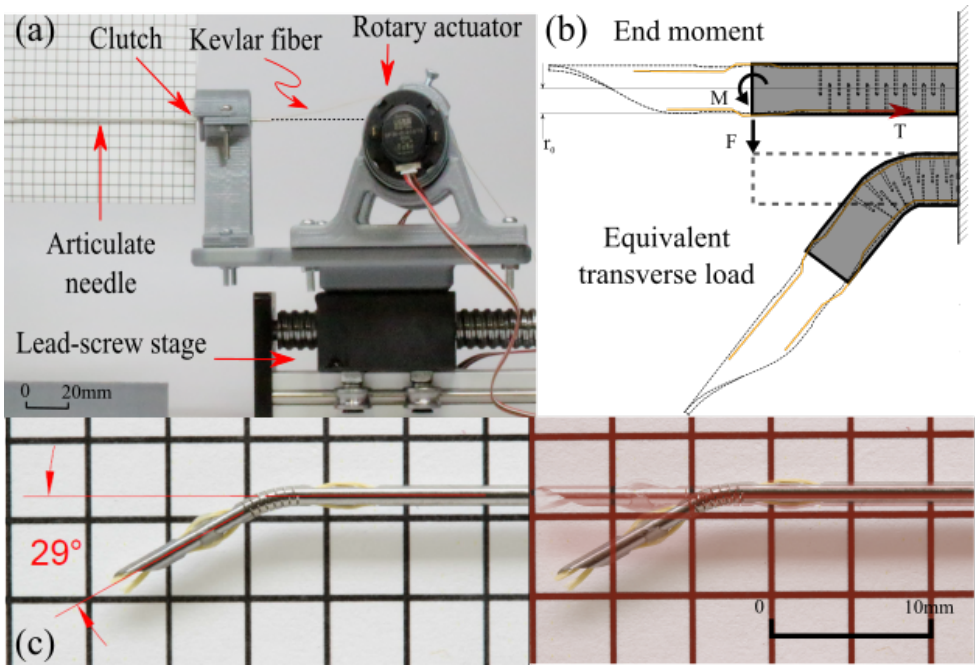

Figure 4.3: (a) Test setup used in experiments. (b) Proposed simplification through equivalent beam deflection models. (c) Observed deflection and planar range of motion for test prototype.

4.2 Needle Tip Mechanics

A modelling assumption is used to idealize the compliant section of the needle joint as a cantilever shown in Fig. 4.3 (b). Here, the tubular sections which precede and succeed the machined region are assumed to be rigid. The tension acting on the tendon is mapped to a comparable transverse tip load. This can be done by modeling the tensile load as an end moment acting on the cantilever beam, where, the torque arm is equal to the outer radius of the NiTi tube. Subsequently, equivalent deflections may be found for a similar section under a transverse tip load as depicted in Fig. 4.3 (b). The tension force has a magnitude T, the inner radius of the cross-section is r_i. Hence, the effective end moment M_{eff} is given as: s

$$M_{eff} = Tr_i \tag{4.10}$$

For a cantilever beam under an end moment or an equivalent transverse tip load (F_{tip}) as previously described, the slope θ is as given by Eq. (22), where E is the elastic modulus of NiTi (83 GPa - austenite), L the length of the beam, and I the cross-sectional moment of inertia for the equivalent section.

$$\theta = \frac{M_{eff}L}{EI} \equiv \frac{F_{tip}L^2}{2EI} \tag{4.11}$$

$$F_{tip} = \frac{2M_{eff}}{L} \tag{4.12}$$

Now, Eq. (23) maps applied tension to an equivalent transverse tip-load (F_{tip}). In our experiments, the strain from the PM-FBG fiber corresponds to applied tension, which in turn provides for an equivalent load, F_{tip}. The magnitude of F_{tip} in air (F_{air}) would differ from that observed within phantom (F_p) due to the contrast in material stiffness and the commensurate measured strain. This difference is attributed to the reaction component from the resultant of the tissue interaction force at the tip, R_t - which is in effect a measure of its compliance. Moreover, the force in air, F_{air} may be determined from the mechanics model outlined previously. Therefore,

$$R_t = F_p - F_{air} \tag{4.13}$$

We further investigate this possibility in Section VI with the aid of Fig. 5.1.

5. PROTOTYPE EVALUATION

The sensorized tendons provide an estimate of stiffness during needle-tissue interactions. This is better understood with the scenario as shown in Fig. 5.1. During insertion - for the given configuration, the reaction force from the phantom opposes flexion in the clockwise direction. Tension on the sensorized tendon is mapped to an equivalent clockwise moment at the distal section based on Eq. (15). This enables flexion in a direction against tissue reaction. The tool design studies described in Section V, further substantiate this idea.

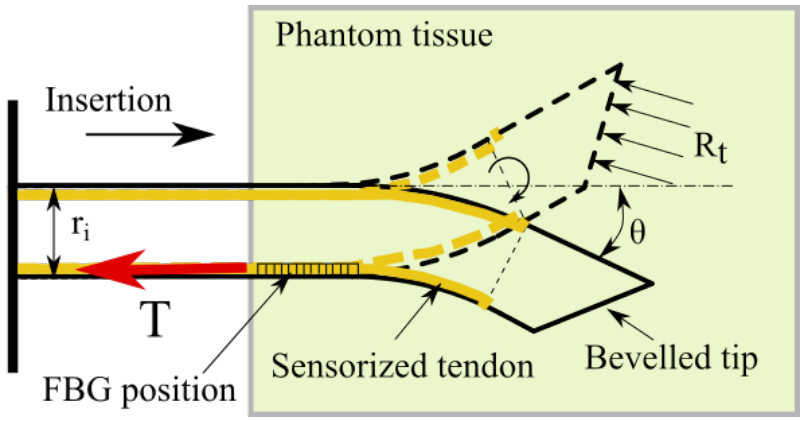

Figure 5.1: Sensorized tendons as a force sensing modality within a steerable needle. During insertion, the resultant tip reaction force (R_t) opposes needle flexion - this is measured as a function of strain given by the PM-FBG fiber using Eq. (24).

Therefore, borrowing from the concepts previously described, the tangential force on the distal segment is a function of applied tension. Hence, the tension required to produce a flexion angle, θ is contingent on phantom compliance. Implicitly, higher the modulus of elasticity, larger the required tension for equivalent angles of flexion (θ). Hence, in

theory, passive instrument bending can be corrected through tendon actuation which in-turn enables stiffness estimation. To substantiate this concept, the subsequent sections present evidence from relevant experiments.

5.1 Tissue Phantom

The sensor instrumented needle prototype was tested within tissue phantoms of varying stiffness. Two materials were used - Plastisol (MF Plastics, Fort Worth, TX) and Medical grade ballistic gelatin (Clear Ballistics Inc., Fort Smith, AK). The plastisol phantoms were fabricated in-house. Phantom compliance is varied by changing the proportions of plastic to thinner in solution. A bench-top compression test apparatus (Instron 5960, Instron Corporation, United Kingdom) was used to determine the elastic moduli.

Phantom Type	**Measured Elastic Modulus (kPa)**
1-1 Plastisol	6.543
2-1 Plastisol	13.540
4-1 Plastisol	22.039
Ballistic gelatin 3	42.084
8-1 Plastisol	57.129
Ballistic gelatin 2	57.711
Plastic phantom	67.111

Table 5.1: Averaged elastic moduli for cubic phantom specimen of side 2.5 in ea. from compression loading experiments at 0.1 in/min and strain margins up to 10%

Phantoms of known dimension were fabricated using standard molds, the specimen were then subject to compressive loads under a consistent strain rate (0.1 in/min). The applied load and corresponding strain were recorded. This way, the elastic modulus for each specimen was determined from the strain-response curves [56]. The averaged strain response for each phantom is as shown on the graph in Fig. 5.2 (a) and the respective elastic moduli are as documented in Table 5.1.

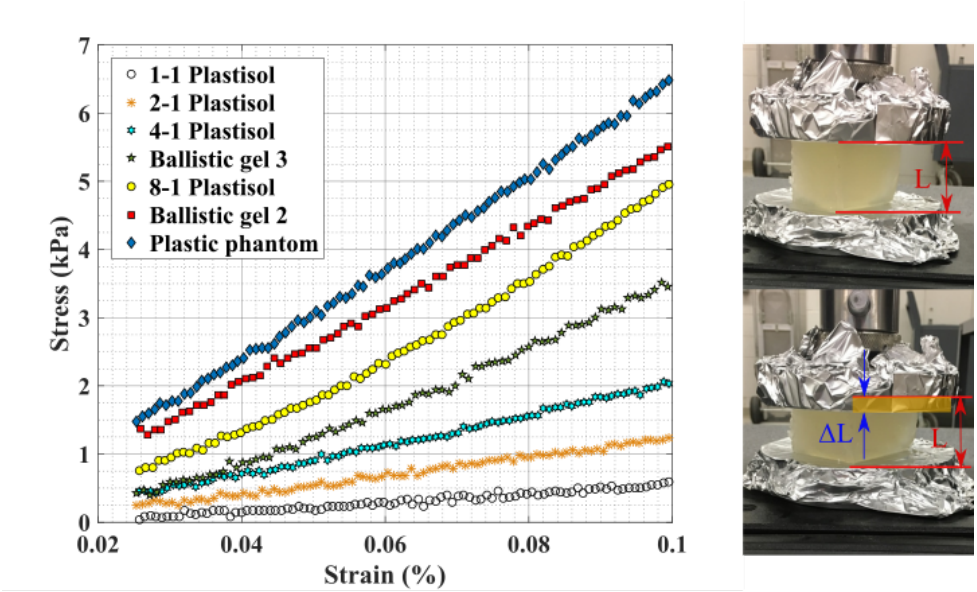

Figure 5.2: (a) Phantom behavior under compressive loading – stress-strain curves to determine elastic moduli. (b) Phantom specimen in compression test setup.

5.2 Behavior Under Static Loads

The PM-FBG fibers are unique in their ability to provide decoupled temperature and strain information. This feature enables real-time estimation of tissue reaction forces using principles outlined previously. To evaluate the functionality of the instrumented prototype in this context, we performed static flexion experiments within different phantom media. The needle was held in place using a 3D printed clutch, and the fibers were pre-tensioned and actuated by antagonistic DC motors. A camera was used to record the observed tip-flexion.

The setup is as shown in FIg. 4.3 (a), the observations show that measured strain is a function of phantom stiffness. This relationship is reasonably linear and lends credence to the argument that strain data may be calibrated to provide a measure for tissue stiffness. Moreover, the difference between observed strain when in air and within phantom provides an estimate for reaction force from tissue during the static experiments (Eq. (24)). With

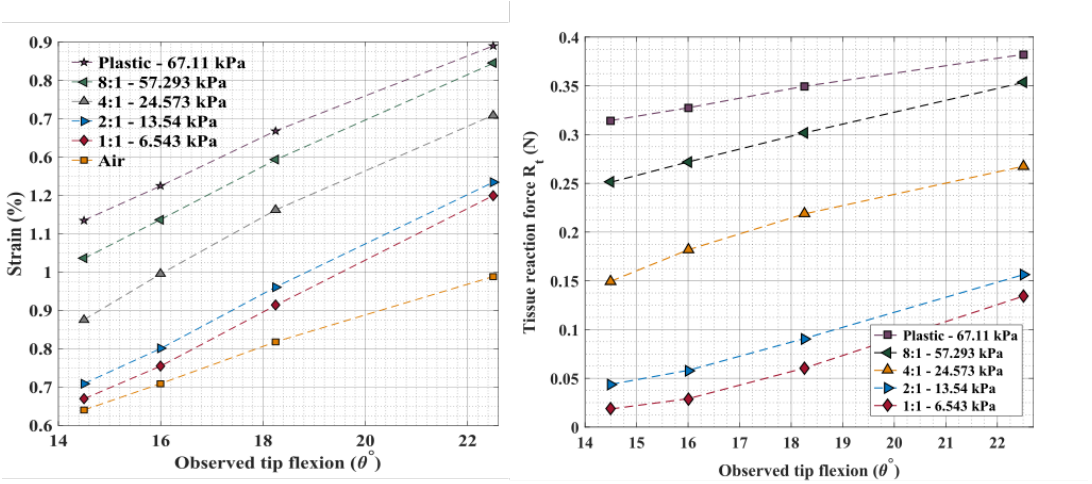

(a) (b)

Figure 5.3: (a) Static flexion experiment: instrumented prototype actuated within different phantom types - strain response and corresponding tip flexion. Ratios correspond to proportion of plastic to thinner in plastisol.(b) Needle tip reaction force as a function of observed flexion angle and phantom stiffness during static actuation experiments. Ratios correspond to proportion of plastic to thinner in plastisol.

focused modeling methods this could provide for force-feedback.

Fig. 5.3 (a) provides a graphical summary of observed strain as a function of tip flexion and its correspondence to phantom stiffness. Clearly, measured strain increases with increase in tip-flexion and (or) phantom stiffness. The assumption that the tendon is inextensible is reinforced from the observation that observed tip flexion is consistent with corresponding pulling length irrespective of the medium used for the test. Intuitively, we notice that higher the stiffness, higher the measured strain for similar extension.

Fig. 5.3 (b) graphically represents the response of reaction force against increasing tip flexion within different phantom media. The force here borrows from the concepts outlined in Section V-B. The reaction force during static experiments is necessarily a consequence of the transverse load acting along the outer wall of the needle cannula which faces the direction of flexion. This force component exhibits an intuitive trend and is a function of phantom compliance. Therefore, the instrument may be calibrated to provide

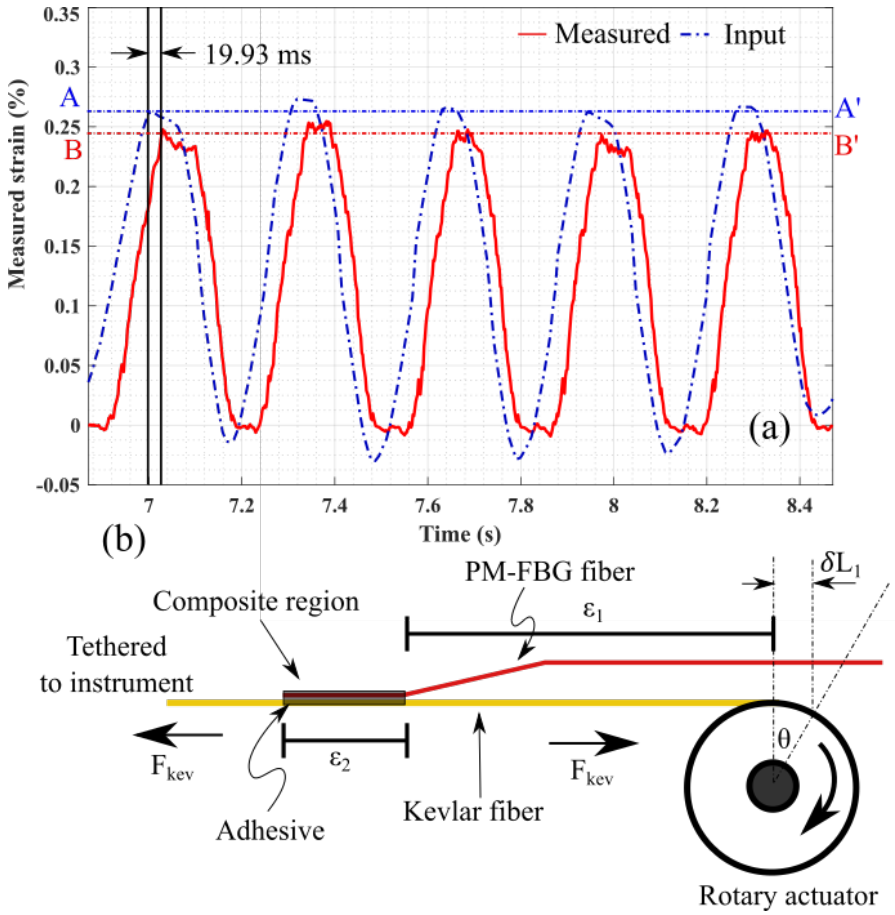

Figure 5.4: (a) Dynamic strain response of the Kevlar-reinforced PM-FBG fiber at a frequency of 1.38 Hz, extension - 1.33 mm and net time - 120 s. Here, AA' corresponds to an approximation for the peak-averaged input strain ε_1 and BB' corresponds to the peak-averaged measured strain ε_2. (b) Composite model of optical fiber within an adhesive substrate for input strain correspondence in Kevlar-reinforced PM-FBG fiber.

for the elastic moduli of tissue during insertion.

5.3 Behavior Under Dynamic Load

Needle steering and the insertion of articulate cannulae are dynamic processes, therefore, although the functionality of the instrument under static conditions is understood, the dynamic behavior of the sensorized tendons could further extend its potential application. In these experiments, pre-tensioned PM-FBG fiber was subject to oscillatory loading

(tension-slack cycles) at different pulling frequencies, length (amplitude), and time accounting for visco-elastic behavior, while their performance was analyzed for consistency in strain response. Here, the frequency of applied load is contingent on actuator RPM (motor speed), the time duration of loading relies on the oscillation count and number of cycles, while the extension is dependent on the angular position of the actuator.

In Fig. 5.4 (a), a section of the strain response corresponding to an extension of 1.33 mm, frequency of 1.38 Hz, and net time interval of 120 s is shown. Evidently, the observed strain as picked up by the Bragg sensors is almost equivalent to the input strain approximation as measured using the optical encoder on the DC motor. Moreover, this relationship is consistent across trials for a given medium (air) and a given prototype as indicated by the amplitude ratio. The observed amplitude ratio is ≈ 0.95. This is better understood with a simple composite model as shown in Fig. 5.4 (b), where ε_1 and ε_2 are the strains across the indicated sections. If the tension applied on Kevlar fiber tethered to the actuator is F_{kev}, and assuming linear behavior across layers, it can be shown that,

$$\frac{F_{Of}}{F_{Kev}} = \frac{F_{Of}}{F_{Ad}} = \frac{E_{Of}}{E_{Ad}} \tag{5.1}$$

F_{Of} and F_{Ad} are the load components borne by the optical fiber and adhesive respectively. E_{Of} and E_{ad} their corresponding moduli of elasticity. For strain compatibility all layers of the composite section undergo equal extensions.

With optical fiber strain ($\varepsilon_{Of} = \varepsilon_2$) as determined by the PM-FBG fibers and with the assumption of complete load transfer between the Kevlar and adhesive (i.e. $F_{Kev} = F_{Ad}$) as a consequence of their contrast in stiffness [57], the strain on the Kevlar fiber ($\varepsilon_{Kev} = \varepsilon_1$) may be determined. In doing so, it is observed that the ratio of strain on the optical fiber to the strain on the Kevlar fiber (i.e. amplitude ratio) is equivalent (using material

properties as detailed in Section IV-B). From the experiments, the amplitude ratio is found to be approx. 0.95, this difference is attributed to the bonding length L_b used during the said trials. An increase in bonding length L_b would further promote strain transfer betweeen the two media.

Notably, there is a response delay between input strain and measured strain to the tune of 20 ms. Table 5.2 provides a complete summary of the observations from the dynamic tests on the instrumented prototype. Interestingly, the observed strain was consistent irrespective of oscillation count (time), RPM (frequency), and varied proportionally with actuation length (extension). It was observed that the fiber response gradually decreases during extended oscillation times, possibly due to the visco-elastic nature of the phantom or fatigue and needs further investigation. However, these intervals are beyond expected operation periods for the application.

5.4 Insertion Tests: Two-layered Phantoms

The performance of the instrument during insertion within two-layered phantom tissue was experimentally investigated. In these trials, the instrumented needle prototype was actuated by a pair of opposed DC motors mounted atop the carriage of a linear ball screw actuator (see Fig. 4.3 (a)). The system allowed for two degrees of freedom - linear insertion, and distal flexion of the needle tip. The instrument was interfaced with three different phantoms (ballistic gelatin 3 - 42.084 kPa, 2:1 plastisol - 13.54 kPa and 1:1 plastisol - 6.543 kPa) in pairs of two. At the outset, the immediate concerns were to ensure that system response was consistent, independent of insertion velocity, phantom arrangement or flexion, and in agreement with strain estimates observed during the static trials.

The stages of insertion are described as follows - first, the needle is oriented in the preferred direction and locked in place by the clutch. The tendons are then tethered to the actuators and provided a fixed (consistent) pre-tension. The required flexion and insertion

Changing oscillation count - Time				
Trial no.	**T1**	**T2**	**T3**	**T4**
Pulling length (mm)	***1.77***			
Motor Speed (RPM)	***9.5***			
Measured strain ε_2 (%)	0.298	0.292	0.299	0.309
Amplitude ratio	0.9426	0.9524	0.9347	0.9834
No. of oscillations	20	30	40	50
Frequency (Hz)	2.857	2.616	2.761	2.730
Response delay (ms)	17.76	18.61	17.88	18.32
Changing pulling length - Extension				
Pulling length (mm)	2.22	1.77	1.33	0.8
Motor Speed (RPM)	***9.5***			
Measured strain ε_2 (%)	0.359	0.298	0.239	0.178
Amplitude ratio	0.9411	0.9767	0.9336	0.9426
No. of oscillations	***20***			
Frequency (Hz)	2.857	1.744	1.380	1.092
Response delay (ms)	18.92	17.76	19.93	10.21
Changing motor speed - Frequency				
Pulling length (mm)	***1.77***			
Motor Speed (RPM) 9	11	13.6	16.7	
Measured strain ε_2 (%) 0.308	0.303	0.307	0.306	
Amplitude ratio 0.9677	0.9720	0.9608	0.9366	
No. of oscillations	***50***			
Frequency (Hz)2.730	3.265	4.075	5.090	
Response delay (ms)18.32	15.23	19.11	17.16	

Table 5.2: A summary of strain response from dynamic tension-slack tests on the instrumented prototype for three scenarios: (a) changing oscillation count - time (up to 200s) (b) increasing extension length - amplitude ($0.89 - 2.25$ mm) (c) actuator RPM - frequency (up to 5 Hz). Measured strain corresponds to peak averaged values over multiple cycles.

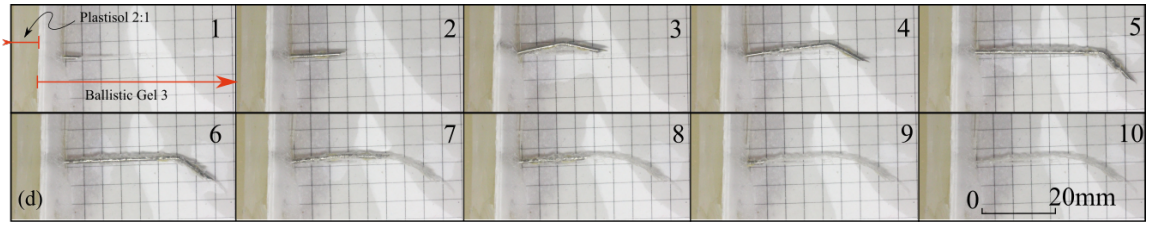

Figure 5.5: An example of the stages of insertion into two phantom layers - from platisol 2:1 segment into ballistic gel 3 segment. Steps [1-5]: insertion, [6-10]: retraction. Frame (10) shows tool path through the clear phantom layer while Frame (3) shows the beginning of tool-flexion.

depths are then fed to the control loop. Subsequently, the needle is inserted within the first phantom layer up to a depth of 20 mm. At this point, strain data is logged by the interrogator. The needle is then actuated by the DC motor to produce the required flexion, followed by a second stage of insertion up to a maximum depth of 80 mm. During this insertion stage the fiber tensions are balanced so as to maintain a consistent tip flexion angle. Finally, slack is introduced to both fibers while data-logging is terminated at the interrogator. The needle is then gradually retracted from within the phantom layers. These stages are depicted visually in Fig. 5.5, where frames [1-5] correspond to insertion, with flexion beginning at frame 3. While, frames [6-10] correspond to tool retraction.

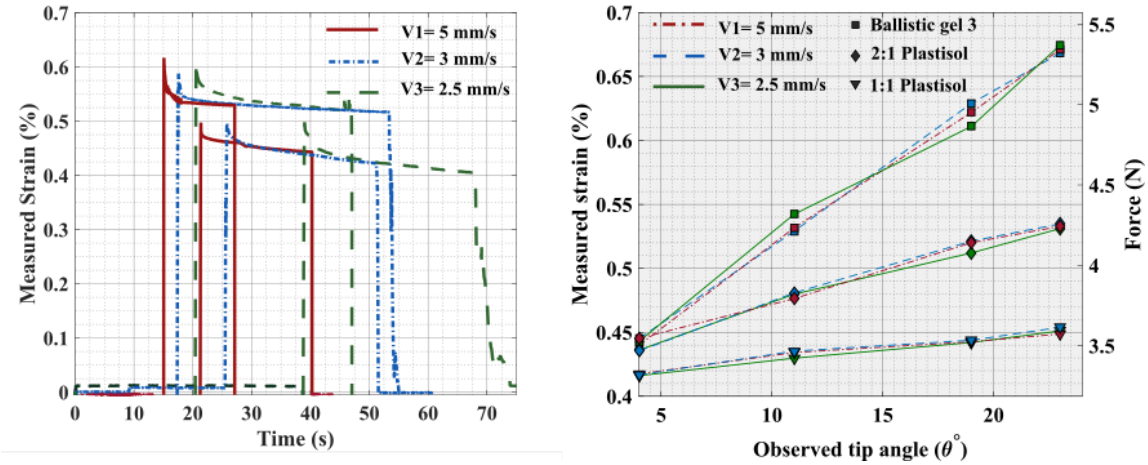

Figure 5.6: Phantom insertion experiments. (a) Single layer insertion into clear ballistic gelatin phantom at three insertion velocities and two angles of flexion. (b) Single layer insertion: strain response as a function of flexion angle under varying insertion speeds and phantom moduli.

The prototype was first inserted into single phantom layers up to a depth of 70 mm, these trials were repeated with changing insertion velocity and tip-flexion angle. In Fig 5.6 (a), the strain response corresponding to insertion within ballistic gelatin is presented for two different angles of tip flexion (11° and 4°) at three different insertion velocities (range:

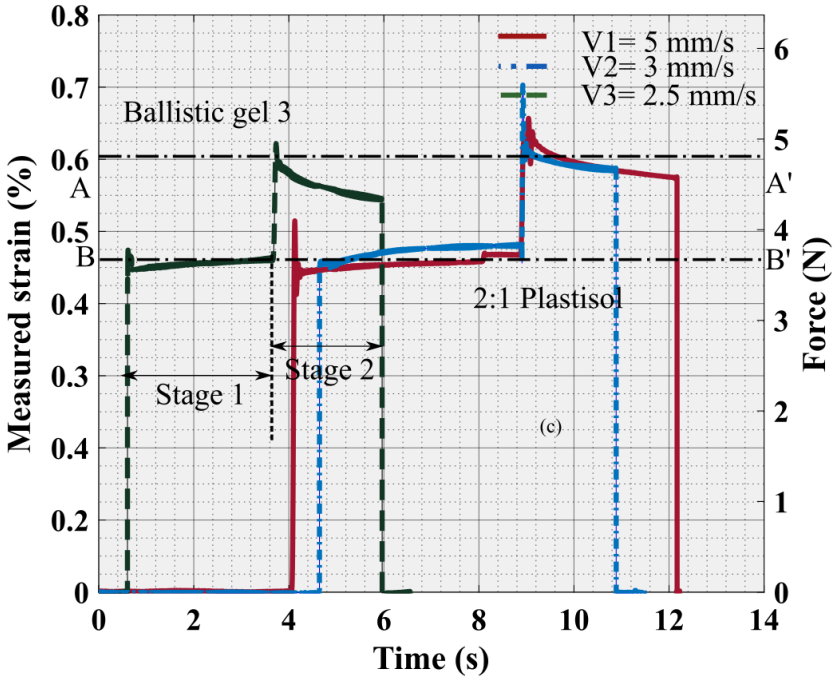

Figure 5.7: Insertion into two phantom layers at three insertion velocities and constant flexion angle.

$2.5 - 5$ mm/s). It was observed that the recorded strain was independent of insertion velocity for the ranges so tested, this is evidenced by the consistent strain peaks depicted on the graph – an attribute common to over 40 trials that were performed within a single phantom layer. At an angle of 11° the measured strain averaged at 0.559% while at an angle of 4° it was 0.4569%. In Fig. 5.6 (b), the peak-averaged strain value corresponding to flexion angle for each phantom type is shown. This data is the average of four trials, at four angles of flexion, within three phantom variants and at three insertion velocities. From the graph, the response agrees with the linear trend observed during earlier experiments (see Fig. 3.1).

Subsequently, the instrument was interfaced with two-layered phantom arrangements starting with insertion into the more compliant region followed by flexion and insertion

into a stiffer segment. The results from a set of insertion trials within two phantom layers is presented in Fig. 5.7, and shows insertion into the 2:1 plastisol segment (Stage-1) followed by insertion into the ballistic gelatin segment (Stage-2) under a flexion angle of 11°.

The observed strain is approximately equivalent to values observed under the single layer phantom experiments. This was reasonably consistent across similar (increasing stiffness) phantom arrangements. Interestingly, the strain behavior corresponds with the expected stress-relaxation of the visco-elastic phantom and could potentially result in an improved tissue modeling strategy. From our observations in Fig. 5.7 it is evident that the instrumented prototype has a stiffness sensitivity of approximately $0.003\%/kPa$ i.e. $35.65\ pm/kPa$ (standard FBG sensitivity is $\sim 1.18pm/\mu\epsilon$) for the given flexion angle.

6. CONCLUSIONS

In this study, we explored a bi-modal approach to sensing and actuation in the form of sensorized tendons using Kevlar-reinforced PM-FBG fibers. Further, a potential application in the form of an articulate robotic needle with stiffness estimation capabilities was discussed to substantiate this proposition. The experiments primarily dwell on the performance of the tendon on its own regard followed by trials to validate its function within the context of the recommended application.

Evidence suggests that the tendons are able to transmit loads up to 40 N, which is substantively more than previously documented for standard optical fibers (no FBG). Besides, they provide for temperature independent strain measurements and means for friction compensation.

When instrumented within the prototype needle, their response to static loads is consistent, linear, and a function of phantom compliance, and flexion angle. This attribute further extends to dynamic loading conditions, where, the documented strain is independent of loading frequency, amplitude and time. Together, these factors add to the stiffness sensing capabilities of the instrument given the nature of tool-tissue interactions during surgery.

This is experimentally validated using the observations from the phantom tissue insertion experiments. Where, the documented strain agrees with those observed under static and dynamic loading conditions and is independent of insertion velocity. Moreover, the response mimics the stress-relaxation behavior of the visco-elastic phantom, and could therefore enable improved tissue modelling approaches.

Hence, with emphasis on force-modeling techniques, dual sensorized actuating tendons, active closed-loop control with online stiffness estimation to ensure a consistent an-

gle of flexure during the insertion stages, and a custom inner PTFE lumen - the proposed concept could potentially fulfill the force-sensing needs of instruments in robot-assisted invasive procedures of today.

REFERENCES

[1] R. H. Taylor, A. Menciassi, G. Fichtinger, and P. Dario, "Medical robotics and computer-integrated surgery," in *Springer handbook of robotics*, pp. 1199–1222, Springer Berlin Heidelberg, 2008.

[2] M. Daouadi, A. H. Zureikat, M. S. Zenati, H. Choudry, A. Tsung, D. L. Bartlett, S. J. Hughes, K. K. Lee, A. J. Moser, and H. J. Zeh, "Robot-assisted minimally invasive distal pancreatectomy is superior to the laparoscopic technique," *Annals of surgery*, vol. 257, no. 1, pp. 128–132, 2013.

[3] F. Corcione, C. Esposito, D. Cuccurullo, A. Settembre, N. Miranda, F. Amato, F. Pirozzi, and P. Caiazzo, "Advantages and limits of robot-assisted laparoscopic surgery: preliminary experience," *Surgical Endoscopy and Other Interventional Techniques*, vol. 19, no. 1, pp. 117–119, 2005.

[4] G. Tholey, J. P. Desai, and A. E. Castellanos, "Force feedback plays a significant role in minimally invasive surgery: results and analysis," *Annals of surgery*, vol. 241, no. 1, pp. 102–109, 2005.

[5] C. Wagner, N. Stylopoulos, and R. Howe, "Force feedback in surgery: Analysis of blunt dissection," in *Proceedings of the 10th symposium on haptic interfaces for virtual environment and teleoperator systems*, 2002.

[6] C. E. Reiley, T. Akinbiyi, D. Burschka, D. C. Chang, A. M. Okamura, and D. D. Yuh, "Effects of visual force feedback on robot-assisted surgical task performance," *The Journal of thoracic and cardiovascular surgery*, vol. 135, no. 1, pp. 196–202, 2008.

[7] D.-H. Lee, U. Kim, T. Gulrez, W. J. Yoon, B. Hannaford, and H. R. Choi, "A laparoscopic grasping tool with force sensing capability," *IEEE/ASME Transactions*

on Mechatronics, vol. 21, no. 1, pp. 130–141, 2016.

[8] A. Trejos, R. Patel, M. Naish, A. Lyle, and C. Schlachta, "A sensorized instrument for skills assessment and training in minimally invasive surgery," *Journal of Medical Devices*, vol. 3, no. 4, p. 041002, 2009.

[9] C. He, S. Wang, H. Sang, J. Li, and L. Zhang, "Force sensing of multiple-dof cable-driven instruments for minimally invasive robotic surgery," *The International Journal of Medical Robotics and Computer Assisted Surgery*, vol. 10, no. 3, pp. 314–324, 2014.

[10] J. Rosen, B. Hannaford, C. G. Richards, and M. N. Sinanan, "Markov modeling of minimally invasive surgery based on tool/tissue interaction and force/torque signatures for evaluating surgical skills," *IEEE transactions on Biomedical Engineering*, vol. 48, no. 5, pp. 579–591, 2001.

[11] S. Elayaperumal, J. H. Bae, B. L. Daniel, and M. R. Cutkosky, "Detection of membrane puncture with haptic feedback using a tip-force sensing needle," in *Intelligent Robots and Systems (IROS 2014), 2014 IEEE/RSJ International Conference on*, pp. 3975–3981, IEEE, 2014.

[12] A. Gijbels, E. B. Vander Poorten, P. Stalmans, and D. Reynaerts, "Development and experimental validation of a force sensing needle for robotically assisted retinal vein cannulations," in *2015 IEEE International Conference on Robotics and Automation. Proceedings. ICRA '15*, pp. 2270–2276, IEEE, 2015.

[13] U. Seibold, B. Kubler, and G. Hirzinger, "Prototype of instrument for minimally invasive surgery with 6-axis force sensing capability," in *2005 IEEE International Conference on Robotics and Automation. Proceedings. ICRA '05*, pp. 496–501, IEEE, 2005.

[14] M. B. Hong and Y.-H. Jo, "Design and evaluation of 2-dof compliant forceps with force-sensing capability for minimally invasive robot surgery," *IEEE Transactions on Robotics*, vol. 28, no. 4, pp. 932–941, 2012.

[15] M. A. Qasaimeh, S. Sokhanvar, J. Dargahi, and M. Kahrizi, "Pvdf-based microfabricated tactile sensor for minimally invasive surgery," *Journal of Microelectromechanical Systems*, vol. 18, no. 1, pp. 195–207, 2009.

[16] U. Kim, D.-H. Lee, W. J. Yoon, B. Hannaford, and H. R. Choi, "Force sensor integrated surgical forceps for minimally invasive robotic surgery," *IEEE Transactions on Robotics*, vol. 31, no. 5, pp. 1214–1224, 2015.

[17] A. Trejos, R. Patel, and M. Naish, "Force sensing and its application in minimally invasive surgery and therapy: a survey," *Proceedings of the Institution of Mechanical Engineers, Part C: Journal of Mechanical Engineering Science*, vol. 224, no. 7, pp. 1435–1454, 2010.

[18] H. M. Le, T. N. Do, and S. J. Phee, "A survey on actuators-driven surgical robots," *Sensors and Actuators A: Physical*, vol. 247, pp. 323–354, 2016.

[19] G. Palli, G. Borghesan, and C. Melchiorri, "Tendon-based transmission systems for robotic devices: Models and control algorithms," in *2009 IEEE International Conference on Robotics and Automation. Proceedings. ICRA '09*, pp. 4063–4068, IEEE, 2009.

[20] S. Jacobsen, E. Iversen, D. Knutti, R. Johnson, and K. Biggers, "Design of the utah/mit dextrous hand," in *Proceedings from the IEEE International Conference on Robotics and Automation, 1986*, vol. 3, pp. 1520–1532, IEEE, 1986.

[21] H. Kobayashi, K. Hyodo, and D. Ogane, "On tendon-driven robotic mechanisms with redundant tendons," *The International Journal of Robotics Research*, vol. 17, no. 5,

pp. 561–571, 1998.

[22] C. Poon, H. Yang, K. Lau, W. Xu, Y. Yam, J. Lau, and P. Chiu, "A bioinspired flexible robot with hybrid actuation mechanisms for endoscopic surgery," in *The Hamlyn Symposium on Medical Robotics*, p. 81, 2014.

[23] P. J. Johnson, C. M. R. Serrano, M. Castro, R. Kuenzler, H. Choset, S. Tully, and U. Duvvuri, "Demonstration of transoral surgery in cadaveric specimens with the medrobotics flex system," *The Laryngoscope*, vol. 123, no. 5, pp. 1168–1172, 2013.

[24] C. Seneci, J. Shang, and G. Yang, "Design of a bimanual end-effector for an endoscopic surgical robot," in *The Hamlyn Symposium on Medical Robot*, 2014.

[25] Y.-L. Park, S. Elayaperumal, B. Daniel, S. C. Ryu, M. Shin, J. Savall, R. J. Black, B. Moslehi, and M. R. Cutkosky, "Real-time estimation of 3-d needle shape and deflection for mri-guided interventions," *IEEE/ASME Transactions On Mechatronics*, vol. 15, no. 6, pp. 906–915, 2010.

[26] J. Van Roosbroeck, S. Ibrahim, E. Lindner, K. Schuster, and J. Vlekken, "Stretching the limits for the decoupling of strain and temperature with fbg based sensors," in *International Conference on Optical Fibre Sensors (OFS24)*, pp. 96343S–96343S, International Society for Optics and Photonics, 2015.

[27] D. R. Berg, T. P. Kinney, P. Y. Li, and A. G. Erdman, "Determination of surgical robot tool force requirements through tissue manipulation and suture force measurement," *Transactions of the ASME-W-Journal of Medical Devices*, vol. 5, no. 2, p. 027517, 2011.

[28] C. Wei, C.-C. Ye, S. W. James, R. P. Tatam, and P. E. Irving, "The influence of hydrogen loading and the fabrication process on the mechanical strength of optical fibre bragg gratings," *Optical Materials*, vol. 20, no. 4, pp. 241–251, 2002.

[29] D.-H. Kang, S.-O. Park, C.-S. Hong, and C.-G. Kim, "Mechanical strength characteristics of fiber bragg gratings considering fabrication process and reflectivity," *Journal of intelligent material systems and structures*, vol. 18, no. 4, pp. 303–309, 2007.

[30] C. Davis, S. Tejedor, I. Grabovac, J. Kopczyk, and T. Nuyens, "High-strain fiber bragg gratings for structural fatigue testing of military aircraft," *Photonic Sensors*, vol. 2, no. 3, pp. 215–224, 2012.

[31] S. J. Mihailov, D. Grobnic, C. W. Smelser, P. Lu, R. B. Walker, and H. Ding, "Bragg grating inscription in various optical fibers with femtosecond infrared lasers and a phase mask," *Optical Materials Express*, vol. 1, no. 4, pp. 754–765, 2011.

[32] Z. Gu, Y. Xu, and K. Gao, "Optical fiber long-period grating with solgel coating for gas sensor," *Optics letters*, vol. 31, no. 16, pp. 2405–2407, 2006.

[33] M. W. Rothhardt, C. Chojetzki, and H. R. Mueller, "High-mechanical-strength single-pulse draw tower gratings," in *Photonics North*, pp. 127–135, International Society for Optics and Photonics, 2004.

[34] S. K. Ibrahim, M. Farnan, D. M. Karabacak, and J. M. Singer, "Enabling technologies for fiber optic sensing," in *SPIE Photonics Europe*, pp. 98990Z–98990Z, International Society for Optics and Photonics, 2016.

[35] S. K. Ibrahim, J. Van Roosbroeck, J. O'Dowd, B. Van Hoe, E. Lindner, J. Vlekken, M. Farnan, D. M. Karabacak, and J. M. Singer, "Interrogation and mitigation of polarization effects for standard and birefringent fbgs," in *SPIE Commercial+ Scientific Sensing and Imaging*, pp. 98520H–98520H, International Society for Optics and Photonics, 2016.

[36] P. Puangmali, K. Althoefer, L. D. Seneviratne, D. Murphy, and P. Dasgupta, "State-of-the-art in force and tactile sensing for minimally invasive surgery," *IEEE Sensors*

Journal, vol. 8, no. 4, pp. 371–381, 2008.

[37] O. Van der Meijden and M. Schijven, "The value of haptic feedback in conventional and robot-assisted minimal invasive surgery and virtual reality training: a current review," *Surgical endoscopy*, vol. 23, no. 6, pp. 1180–1190, 2009.

[38] H. Xin, J. Zelek, and H. Carnahan, "Laparoscopic surgery, perceptual limitations and force: A review," in *First Canadian student conference on biomedical computing*, vol. 144, 2006.

[39] K. Harada, K. Tsubouchi, M. G. Fujie, and T. Chiba, "Micro manipulators for intrauterine fetal surgery in an open mri," in *2005 IEEE International Conference on Robotics and Automation. Proceedings. ICRA '05*, pp. 502–507, IEEE, 2005.

[40] J. H. Lee, W. H. Shin, and D.-S. Kwon, "A modularized wire-driven overtube using tube type bending mechanism for robotic notes system," in *Control, Automation and Systems (ICCAS), 2013 13th International Conference on*, pp. 631–634, IEEE, 2013.

[41] G. S. Guthart and J. K. Salisbury, "The intuitive/sup tm/telesurgery system: overview and application," in *2000 IEEE International Conference on Robotics and Automation. Proceedings. ICRA '00*, vol. 1, pp. 618–621, IEEE, 2000.

[42] R. M. Ohline, J. M. Tartaglia, A. Belson, A. T. Roth, W. A. Keller, S. C. Anderson, and C. A. Julian, "Tendon-driven endoscope and methods of insertion," Feb. 22 2005. US Patent 6,858,005.

[43] P. W. Chiu, S. Phee, Z. Wang, Z. Sun, C. C. Poon, T. Yamamoto, I. Penny, J. Y. Wong, J. Y. Lau, and K. Ho, "Feasibility of full-thickness gastric resection using master and slave transluminal endoscopic robot and closure by overstitch: a preclinical study," *Surgical endoscopy*, vol. 28, no. 1, pp. 319–324, 2014.

[44] N. J. van de Berg, D. J. van Gerwen, J. Dankelman, and J. J. van den Dobbelsteen, "Design choices in needle steeringâĂŤa review," *IEEE/ASME Transactions on Mechatronics*, vol. 20, no. 5, pp. 2172–2183, 2015.

[45] S. P. DiMaio and S. E. Salcudean, "Needle steering and motion planning in soft tissues," *IEEE Transactions on Biomedical Engineering*, vol. 52, no. 6, pp. 965–974, 2005.

[46] R. J. Webster III, J. S. Kim, N. J. Cowan, G. S. Chirikjian, and A. M. Okamura, "Nonholonomic modeling of needle steering," *The International Journal of Robotics Research*, vol. 25, no. 5-6, pp. 509–525, 2006.

[47] P. E. Dupont, J. Lock, B. Itkowitz, and E. Butler, "Design and control of concentric-tube robots," *IEEE Transactions on Robotics*, vol. 26, no. 2, pp. 209–225, 2010.

[48] T. R. Wedlick and A. M. Okamura, "Characterization of pre-curved needles for steering in tissue," in *Engineering in Medicine and Biology Society, 2009. EMBC 2009. Annual International Conference of the IEEE*, pp. 1200–1203, IEEE, 2009.

[49] S. Y. Ko, L. Frasson, and F. R. y Baena, "Closed-loop planar motion control of a steerable probe with a programmable bevel inspired by nature," *IEEE Transactions on Robotics*, vol. 27, no. 5, pp. 970–983, 2011.

[50] F. Pigeon, S. Pelissier, A. Mure-Ravaud, H. Gagnaire, and C. Veillas, "Optical fibre young modulus measurement using an optical method," *Electronics Letters*, vol. 28, no. 11, pp. 1034–1035, 1992.

[51] H. Cease, P. Derwent, H. Diehl, J. Fast, and D. Finley, "Measurement of mechanical properties of three epoxy adhesives at cryogenic temperatures for ccd construction," *Fermi National Accelerator Laboratory*, 2006.

[52] M. Kaneko, T. Yamashita, and K. Tanie, "Basic considerations on transmission characteristics for tendon drive robots," in *Advanced Robotics, 1991.'Robots in Unstructured Environments', 91 ICAR., Fifth International Conference on*, pp. 827–832, IEEE, 1991.

[53] P. J. Swaney, P. A. York, H. B. Gilbert, J. Burgner-Kahrs, and R. J. Webster, "Design, fabrication, and testing of a needle-sized wrist for surgical instruments," *Journal of Medical Devices*, vol. 11, no. 1, p. 014501, 2017.

[54] R. Wilfong and J. Zimmerman, "Strength and durability characteristics of kevlar aramid fiber," in *Journal of Applied Polymer Science: Applied Poymer Symposium*, vol. 31, pp. 1–21, 1977.

[55] D. B. Camarillo, C. F. Milne, C. R. Carlson, M. R. Zinn, and J. K. Salisbury, "Mechanics modeling of tendon-driven continuum manipulators," *IEEE Transactions on Robotics*, vol. 24, no. 6, pp. 1262–1273, 2008.

[56] R. Stockwell, "Biological materials: Structure, mechanical properties and modeling of soft tissues," *Journal of anatomy*, vol. 160, p. 234, 1988.

[57] S. C. Ryu, Z. F. Quek, P. Renaud, R. J. Black, B. L. Daniel, and M. R. Cutkosky, "An optical actuation system and curvature sensor for a mr-compatible active needle," in *2012 IEEE International Conference on Robotics and Automation. Proceedings. ICRA '12*, pp. 1589–1594, IEEE, 2012.